Construction and Building Materials 485 (2025) 141898

Contents lists available at ScienceDirect

Construction and Building Materials

journal homepage: www.elsevier.com/locate/conbuildmat

Pull-out behavior of novel spherical-end steel fibers in zirconium oxide nanoparticle-enhanced ultra-high-performance concrete

Hakan Çağlar

Faculty of Engineering and Architecture, Department of Civil Engineering, Kırşehir Ahi Evran University, Kırşehir, Turkey

ARTICLE INFO

Keywords:
Spherical-end steel fibers
Pull-out behavior
Ultra-high-performance concrete (UHPC)
Zirconium OXide Nanoparticles
Multi-scale modeling
Flexural strength

ABSTRACT

This study introduces a novel steel fiber with spherical ends, designed to enhance mechanical interlocking in ultra-high-performance concrete (UHPC) matrices. The UHPC was further reinforced with zirconium oxide (ZrO_2) nanoparticles to improve its mechanical properties. A nonlinear finite element method (FEM), along with a multiscale modeling approach, was used to simulate fiber pull-out and flexural behavior. Experimental tests, including compressive and tensile strength measurements, were conducted to calibrate and validate the numerical models. Results show that the optimal nanoparticle content is 1.0 wt%, which increased compressive and tensile strengths by 37 % and 38 %, respectively. Compared to straight fibers, the spherical-end fibers exhibited significantly improved performance, with a 124 % increase in pull-out force and a 188 % increase in pull-out energy. In three-point bending tests, UHPC specimens with 2 vol% spherical-end fibers showed a 214 % increase in flexural strength over plain UHPC and about 102 % over those with straight fibers. These results underscore the effectiveness of spherical-end fibers in improving the toughness and load-bearing capacity of UHPC, making them highly suitable for high-performance structural applications.

1. Introduction

UHPC is recognized as an advanced material in various construction productions due to its exceptional mechanical properties and durability [1,2]. The adding of steel fibers shows a critical role in enhancing the flexural strength, tensile strength, and crack control of this type of concrete. In this regard, the pull-out behavior of steel fibers, which represents the mechanical interaction between the fibers and the concrete matrix, is a key factor in improving the overall mechanical performance of fiber-reinforced concrete. As a result, the development of various fiber geometries and materials has attracted significant interest from researchers [3].

The advancement of high-performance cementitious composites has spurred substantial research into novel fiber reinforcement strategies, with spherical-end steel fibers emerging as a promising alternative to conventional straight fibers. Numerous studies have highlighted the limitations of traditional straight fibers regarding pull-out behavior and efficient stress transfer, prompting investigation into modified fiber geometries [4,5]. Recent efforts have focused on various fabrication techniques for these fibers, including cold forming and casting [6,7]. Experimental studies have characterized their pull-out behavior, examining parameters such as embedment length, fiber diameter, and end geometry [8,9], with researchers using cohesive zone models to numerically simulate interfacial interactions [10,11]. These models have shown improved stress transfer and energy dissipation with spherical-end fibers. In particular, research by Elshinawy et al. [12] demonstrated improved mechanical properties of concrete with end-deformed steel fibers, while Yang et al. [13] further showed that the fiber end geometry had a large effect on the overall mechanical performance. Pull-out studies by Overhage et al. [14] and Chen et al. [15] provide valuable experimental data on the influence of fiber geometry and embedment length. Finite Element examination was used by Pouraminian et al. [16] in the development of a cohesive zone model that is particularly suitable for recycled steel fibers.

Research on mechanical properties of composites has exposed that these fibers can substantially increase both flexural strength and toughness [17]. Furthermore, research by Que et al. [18] and Bao et al. [19] confirms significant improvements in flexural performance of concrete reinforced with such fibers. Research by Gu et al. [20] further explored the impact resistance of concrete with such fibers, demonstrating potential applications in structures under dynamic loading. Ongoing efforts focus on incorporating nanomaterials to further improve mechanical and durability characteristics of these composites. Li et al. [21] observed synergistic effects of nano-silica and hook-end

E-mail address: c.hakan@ahievran.edu.tr.

https://doi.org/10.1016/j.conbuildmat.2025.141898
Received 17 January 2025; Received in revised form 23 April 2025; Accepted 19 May 2025
Available online 27 May 2025

steel fibers on cementitious composites. Studies also explore the interface modification using nanomaterials as a method for improving bond strength [22]. Finally, challenges still exist regarding efficient and cost-effective mass production as well as optimization of geometric parameters for achieving maximum performance of fibers [23,24]. Overall, these studies highlight the importance of continued research into the development, analysis and application of spherical end steel fibers in cementitious composites. To develop optimized steel fibers as strengthening for UHPC, Yoo et al. [25] deliberated three distinct types of steel fibers with varying geometries, namely circular straight and twisted triangular. The surfaces of these steel fibers were further improved through an electrolyte solution containing ethylenediaminetetraacetic acid. In a similar vein, Kim et al. [26] examined the effectiveness of curvilinear steel fibers in enhancing the pullout resistance of conventional straight steel fibers within a UHPC matrix. Zhang et al. [27] introduced a novel stranded steel fiber by simply cutting commercial steel strands. Li et al. [28,29] explored the effects of various fiber volume fractions and end geometries on the pullout behavior of both straight and arc-shaped steel fibers in slurry-infiltrated fiber concrete. Schleiting et al. [30] proposed the application of a thermoplastic elastomer coating for fibers to enhance bonding. Pullout tests with brass-coated steel and stainless steel fibers—both with and without the TPE coating—were conducted, alongside flexural strength tests of UHPC reinforced with the same fibers. Additionally, Ataa et al. [31] explored a novel steel fiber created by twisting two straight steel wires together, investigating its pullout behavior and demonstrating its slip-hardening capability in cement-based matrices. This research underscores the continuous efforts to optimize steel fibers, aiming to enhance pullout resistance, bonding, and overall performance in fiber-reinforced concrete. Ultimately, these advancements contribute to the development of high-strength materials for use in advanced structural applications. Park et al. [32] estimated the pullout resistance performance of a newly developed double-arched steel fiber. Pullout experiments were conducted to evaluate key parameters, such as resistance load, bond strength, and energy absorption capacity, in relation to the geometry and tensile strength of the fibers. These findings demonstrate the superior pullout resistance of double-arched fibers, underscoring their potential to significantly enhance the performance of fiber-reinforced concrete.

Steel fibers are commonly used in UHPC to improve tensile strength and control cracking; however, conventional straight fibers often face challenges that limit their effectiveness. One major issue is fiber slippage under loading, which occurs due to limited mechanical anchorage and insufficient bond strength at the fiber-matrix interface. Additionally, stress concentrations at the fiber ends may lead to premature debonding or even matrix cracking. These shortcomings reduce the full utilization of the fiber tensile capacity and compromise the overall ductility and energy absorption of the composite.

To overcome these limitations, this study introduces a novel steel fiber with spherical ends. The spherical-end design increases the contact area between the fiber and the surrounding concrete matrix, enhancing mechanical interlocking and resisting pull-out more effectively. Moreover, the curved geometry of the ends distributes stresses more uniformly, reducing the likelihood of stress-induced damage at the interface. This design aims to achieve more reliable anchorage, minimize slippage, and ultimately enable the fiber to reach its full tensile potential before failure. The incorporation of nanoparticles into cementitious composites has emerged as a promising strategy for enhancing their mechanical performance, durability, and microstructural integrity. Among various nanomaterials [33–36], zirconium oxide (ZrO_2) nanoparticles are particularly attractive due to their high chemical stability, fine particle size, and strong pozzolanic reactivity. These nanoparticles contribute to improved particle packing, reduced porosity, and accelerated hydration kinetics by acting as nucleation sites for calcium silicate hydrate formation [37–40].

Steel fibers are typically manufactured with smooth or patterned surfaces, but limitations such as slippage or premature rupture under loading reduce their full effectiveness. To address this challenge, this study introduces a novel type of steel fiber with spherical ends. The spherical-end design, due to an increased contact area and improved mechanical interlocking, has the potential to enhance pull-out behavior and increase the load-bearing capacity of the fibers. Alongside this innovation, the use of zirconium oxide (ZrO_2) nanoparticles as a reinforcement in the UHPC matrix provides a basis for further improvement in mechanical properties. By enhancing matrix homogeneity and strengthening the bond between fibers and the matrix, these nanoparticles can play a significant role in improving concrete performance. This study examines the pull-out behavior of novel fibers and their impact on the mechanical properties of UHPC reinforced with zirconium oxide nanoparticles. The main objective is to assess the potential of these fibers to improve the mechanical performance of concrete and compare their effectiveness with conventional steel fibers. The outcomes of this research could contribute to the development of advanced and more efficient materials for use in construction industry.

The structure of the present study is as follows. Section 2 outlines the experimental design, production of specimens, and the procedures for conducting direct tensile, uniaxial compression, fiber pull-out, and three-point bending tests. Section 3 presents the methodology for performing finite element simulations to analyze fiber pull-out behavior and three-point bending. Section 4 focuses on presenting and discussing both experimental and numerical results. Finally, Section 5 provides the conclusions of the study.

2. Experimental procedures

The experimental tests aimed to determine the optimal percentage of zirconium oxide nanoparticles for enhancing the mechanical properties of UHPC. These tests served two primary purposes: (1) to establish the mechanical properties required for finite element analyses and (2) to provide empirical data for validating the results of the FE model.

2.1. Spherical-end steel fibers

This study introduces a novel steel fiber design incorporating spherical ends, presented here for the first time. These fibers are engineered to enhance bond behavior and pull-out performance in UHPC, offering superior mechanical efficiency compared to conventional steel fibers. While conventional fibers are widely used in UHPC, they often suffer from limitations such as slippage within the concrete matrix and premature rupture. By modifying the end geometry to a spherical structure, this research demonstrates significant improvements in the mechanical behavior of the fibers, particularly under tensile and flexural loads. The key advantages of this design include:

1. **Increased Contact Area:** The spherical ends enhance mechanical interlock with the concrete matrix, providing a stronger bond.
2. **Reduction of Stress Concentration:** The spherical shape minimizes stress concentration at the fiber ends, reducing the likelihood of slippage or localized failure.

Fig. 1 shows geometry of spherical-end steel fibers. In this figure, d_f and d_e represent the fiber diameter and the spherical-end diameter, respectively. Fig. 1b provides an example of a spherical-end steel fiber produced using a forming method. The spherical-end steel fibers used in this study had a shaft diameter (d_f) of 0.4 mm. The diameter of the enlarged spherical end (d_e) varied between 0.5 mm and 0.8 mm across different experimental configurations. The embedded length of the fibers was fixed at 10 mm for all pull-out tests. These geometrical parameters were selected based on preliminary simulations to estimate the effect of end anchorage on bond behavior.

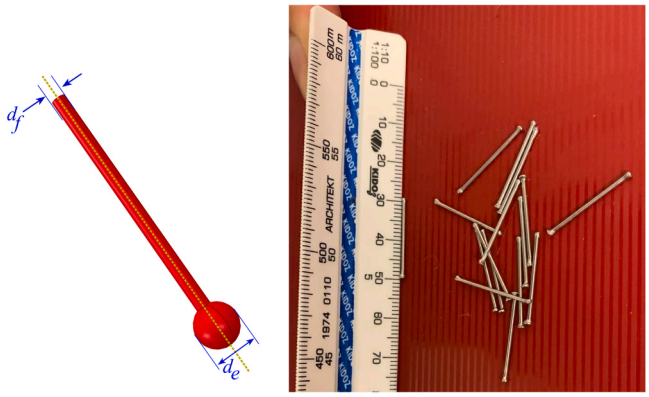

(a) (b)

Fig. 1. Geometry and production of spherical-end steel fibers: (a) schematic representation with fiber diameter (d_f) and spherical-end diameter (d_e); (b) example of a produced spherical-end steel fiber.

2.2. Mix design

To produce UHPC with a compressive strength exceeding 100 MPa, various mix designs were formulated. For each mixture, three $5 \times 5 \times 5$ cm^3 cubic specimens were prepared to determine compressive strength. After casting, the specimens were compacted for 2 minutes on a vibrating table and initially cured under laboratory conditions (ambient temperature of 20 ± 2 °C) for 24 hours. Subsequently, the specimens were demolded and transferred to a moist curing chamber maintained at a temperature of 22 ± 2 °C and relative humidity above 95 %, where they were stored until the designated testing age (7 or 28 days). This curing method was selected to simulate practical curing conditions without relying on elevated-temperature steam curing. The final mix design was selected based on the results of the compressive strength tests, and its details are shown in Table 1. The cement used complied with ASTM C150 standards, and the superplasticizer conformed to ASTM C494-Type D standards. The zirconium oxide nanoparticles, with a purity of 99.9 %, were sourced from US Research Nanomaterials and had an average particle size of 120 nm as shown in Fig. 2.

2.3. Fiber pull-out test

Each pull-out specimen was designed to include only one centrally embedded steel fiber, allowing the isolation of individual fiber-matrix interaction. The dog-bone-shaped geometry and plastic sheet separation (Fig. 3a) ensured controlled debonding at the interface. This setup was intentionally developed to enable direct comparison with the FEM model, which simulates the pull-out behavior of a single fiber. No scaling or data adjustment was required between experimental and numerical results.

The pull-out performance of spherical-end steel fibers was examined using small dog-bone specimens, as shown in Fig. 3a. These specimens featured a cross-section of 25×25 mm^2 and were separated by a thin plastic sheet to facilitate the pull-out test. Three specimens were prepared for each test configuration to obtain average data. During the casting of UHPC reinforced with zirconium oxide nanoparticles, a single fiber was embedded at the center of each dog-bone specimen. Fig. 3b depicts the pull-out test setup. The pull-out tests were performed using an Instron 5965 universal testing machine with a maximum load capacity of 10 kN and load measurement accuracy of ± 0.5 %. Displacement was measured using the machine's built-in LVDT (Linear Variable Differential Transformer), model Instron 2620–601, with a stroke range of ± 25 mm and an accuracy of ± 0.02 mm. The pull-out force was recorded via a Model 2530–50 load cell with a resolution of 0.001 N. Loading was applied under displacement control at a rate of 0.2 mm/min. Displacement control was applied at a rate of 0.2 mm/min. Loading was applied under displacement control at a rate of 0.2 mm/min. Tensile strength tests were performed on specimens containing zirconium oxide nanoparticle concentrations of 0.0, 0.5, 1.0, and 1.5 wt%.

Table 1
Mix proportions of UHPC.

Mix Component	Content (kg/m^3)
Portland Cement Type II	670
Silica Fume	200
Quartz Powder	285
Silica Sand	1020
Superplasticizer (3 %)	20.1
Zirconium Oxide Nanoparticles	0–1.5 wt% of Cement
Water	178

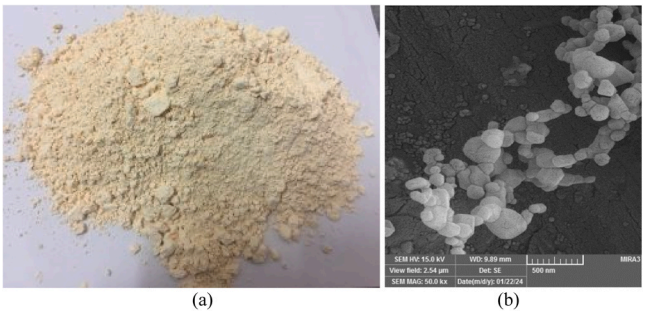

(a) (b)

Fig. 2. (a) Zirconium oxide nanoparticle powder and (b) SEM image of zirconium oxide nanoparticles.

For comparison purposes, conventional straight steel fibers were also tested under the same conditions. These fibers had a nominal diameter of 0.4 mm, an embedded length of 30 mm, and were made of high-carbon steel with a tensile strength of approximately 1180 MPa. The surface of the fibers was smooth and untreated. These parameters were selected to ensure consistency with the spherical-end fibers, allowing for a direct and fair comparison of their pull-out performance.

2.4. Tensile strength test

To define the tensile strength of the UHPC mortar, the briquette tension test, detailed in ASTM C307–03, was employed. Given that ultra-high-performance concrete has a very fine particle size distribution, this test is suitable for obtaining the direct tensile strength of this type of concrete. Dog-bone-shaped specimens with a length of 80 mm and a thickness of 25 mm, as shown in Fig. 4, were fabricated. The mid-section of the specimen has a cross-sectional area of 25 mm × 25 mm^2. Tensile strength tests were conducted using the Instron 5965 UTM, equipped with a Model 2530–50 precision load cell (capacity 10 kN, accuracy ± 0.5 %) and an internal Instron 2620–601 LVDT to capture elongation with an accuracy of ± 0.02 mm. The loading rate was maintained at 0.2 mm/min under displacement control mode. The data acquisition system was calibrated to a sampling rate of 10 Hz. Loading was applied under displacement control at a rate of 0.2 mm/min. Tensile strength tests were performed on specimens containing 0.0, 0.5, 1.0, and 1.5 wt% of zirconium oxide nanoparticles.

2.5. Compressive strength test

The compressive strength test was accompanied on $50 \times 50 \times 50$ mm^3 cubic specimens, according to the ASTM C109/C109M standard. The three-point bending tests were carried out using the same Instron 5965 system, with the load measured by the Model 2530–50 load cell. To accurately capture beam deflection, an external LVDT (Solartron 921994 AX/5.0/S) with a measurement range of ± 5 mm and resolution of 0.005 mm was positioned at mid-span. This

(a) (b)

Fig. 3. Fiber pull-out test setup: (a) dog-bone specimen geometry for pull-out testing; (b) experimental setup for fiber pull-out test.

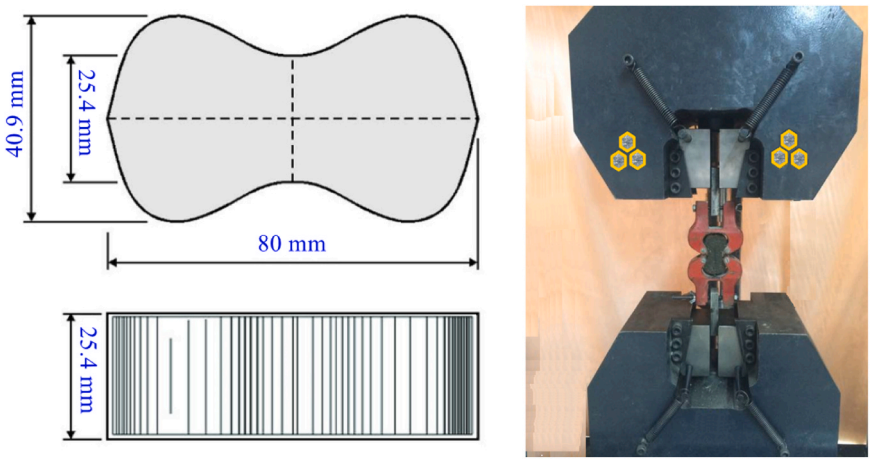

Fig. 4. Direct tensile test setup according to ASTM C307–03.

external LVDT was connected to a Data Translation DT9836 data acquisition module, allowing synchronized high-resolution recording of load and displacement.

Fig. 5 illustrations the specimens used for the compressive strength test. Compressive strength tests were performed on specimens containing 0.0, 0.5, 1.0, and 1.5 wt% of zirconium oxide nanoparticles.

2.6. Flexural strength test

The flexural strength of UHPC containing the novel spherical-end fibers and reinforced with the optimal percentage of zirconium oxide nanoparticles was estimated using a three-point bending test, following ASTM C78 standards. Beam specimens with dimensions of $150 \times 40 \times 40$ mm^3 were tested by applying a load at one-third points along their span. The modulus of rupture was calculated based on load at failure point. The test was performed with a constant displacement rate of 1.0 mm/min. To minimize support settlement and ensure proper positioning, the edges of each specimen were precisely ground using a lapping machine. Fig. 6 illustrates the flexural strength test specimen and the three-point bending experiment setup.

Fig. 5. Specimens used for the compressive strength experiment.

3. Finite element simulation

The finite element method (FEM) is a powerful numerical technique widely used for simulating the mechanical behavior of complex materials and structures under various loading conditions [41–44]. This section details the FE method employed in this work. First, the constitutive equations for concrete are presented. Then, the simulation of the fiber pull-out process is described. Finally, the multiscale FE model used to simulate the three-point bending behavior of ultra-high-performance concrete in the presence of novel spherical-end steel fibers and zirconium oxide nanoparticles is explained.

3.1. Constitutive equations for UHPC containing zirconium oxide nanoparticles

Following the experimental compressive and tensile strength tests, the optimal content of zirconium oxide nanoparticles was determined to be 1.0 wt% ZrO2. Accordingly, finite element simulations were performed on specimens with this nanoparticle content. To simulate the nonlinear mechanical behavior of concrete, the widely used Concrete Damaged Plasticity (CDP) model, available in ABAQUS, was utilized.

(a) (b)

Fig. 6. (a) Flexural strength test specimen; (b) three-point bending test setup.

The CDP model describes the inelastic behavior and failure of concrete through the concept of isotropic damage elasticity in combination with isotropic compressive and tensile plasticity, requiring stress-strain curves under both compression and tension. The stress-strain curves of the plain (cementitious matrix) and zirconium oxide nanoparticle-enhanced UHPC under uniaxial tension and compression were obtained from the experimental tests. The stress-strain curves obtained for the ultra-high-performance concrete containing 1.0 wt% ZrO2 under tension and compression are shown in Fig. 7. According to the ABAQUS user manual, the stress-strain relationships for UHPC must be converted into inelastic stress-strain relationships to be suitable for analysis using the CDP model in ABAQUS. The inelastic strain was calculated using Eqs. (1) and (2). The inelastic stress-strain values for the UHPC are given in Table 2.

$$\varepsilon_c^{in} = \varepsilon - \frac{\sigma_c}{E_c} \tag{1}$$

$$\varepsilon_t^{in} = \varepsilon - \frac{\sigma_t}{E_c} \tag{2}$$

where σ_c and σ_t represent the compressive stress and tensile stress, respectively, and E_c is the elastic modulus of the concrete.

To simulate crack propagation behavior, damage parameters for tension and compression were defined to activate once the peak stress was reached. This approach enabled the FE model to capture the degradation behavior of UHPC under both tensile and compressive loading. The compressive and tensile damage parameters implemented in the model were derived from reference [45] and were calculated using Eqs. (3) and (4) for compression and tension, respectively.

$$D_c = 1 - \frac{\sigma_c E_c^{-1}}{\varepsilon_c^{pl}\left(\frac{1}{b_c} - 1\right) + \sigma_c E_c^{-1}} \tag{3}$$

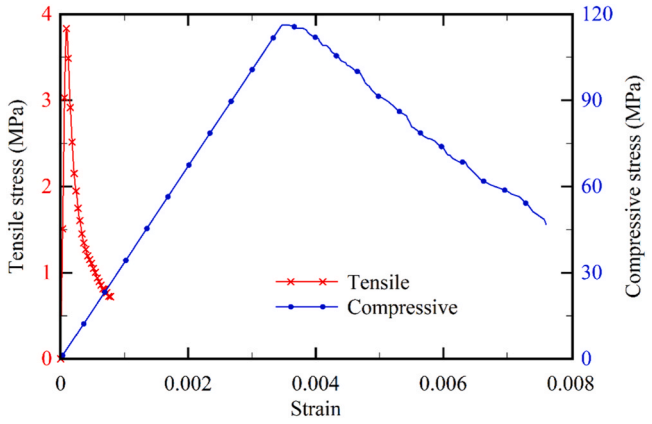

Fig. 7. Uniaxial stress-strain curves of plain and 1 wt% zirconium oxide nanoparticle-enhanced ultra-high-performance concrete.

Table 2
Mechanical properties of 1 wt% zirconium oxide nanoparticle-enhanced ultra-high-performance concrete used in ABAQUS.

Compression behavior			Tension behavior		
Comp. Stress (MPa)	Inelastic strain	Damage parameter (D_c)	Tensile stress, (MPa)	Crack strain	Damage parameter (D_t)
100.86	0	0	3.94	0	0
110.01	0.000253	0.029	3.87	7.51E−06	0.987
114.82	0.000555	0.065	3.54	3.67E−05	0.991
113.09	0.00136	0.153	2.45	0.000172	0.993
90.31	0.002158	0.245	1.89	0.000234	0.994
75.96	0.002974	0.335	1.42	0.000325	0.996
56.74	0.004504	0.494	1.24	0.000359	0.997
48.23	0.005222	0.557	0.98	0.000546	0.997
39.31	0.00664	0.653	0.72	0.000751	0.998
28.36	0.007577	0.736	0.67	0.000874	0.999
19.38	0.008381	0.760	0.59	0.001056	0.999

$$D_t = 1 - \frac{\sigma_t E_c^{-1}}{\varepsilon_t^{pl}\left(\frac{1}{b_t} - 1\right) + \sigma_t E_c^{-1}} \tag{4}$$

where D_c and D_t are the damage parameters of concrete in compression and tension, respectively, and $\varepsilon pl,c$ and $\varepsilon pl,t$ are the plastic strains corresponding to the compressive and tensile stresses. According to Bahij et al. [46], the values of b_c and b_t were selected as 0.7 and 0.1, respectively.

In addition, the CDP model requires five additional parameters: the flow potential eccentricity (ε), the viscosity parameter that defines viscoplastic regularization (μ), the ratio of the second stress invariant on the tensile meridian to the second stress invariant on the compressive meridian such that the maximum principal stress is negative (K_c), the ratio of the initial biaxial compressive yield stress to the initial uniaxial compressive yield stress (σ_{b0}/σ_{c0}), and the dilation angle in degrees (Ψ). For UHPC, these parameters were defined as 0.1, 0.0, 0.68, 1.15, and 20°, respectively, after calibrating the numerical and experimental results for the uniaxial tension and compression tests. Furthermore, the elastic modulus for UHPC was set to 35.6 GPa in the FE models.

3.2. Mechanical behavior of fibers

The steel fibers were modeled in ABAQUS using a metal plasticity model that accounted for both hardening and damage behavior. The stress-strain relationship of the fibers was input into the software as a piecewise linear function, with the elastic modulus, yield strength, and hardening parameters determined from experimental data. The mechanical properties of the steel fibers are summarized in Table 3. To represent damage, a tensile strain-based damage criterion was incorporated. This allowed the model to simulate the gradual degradation of the fibers under high loading conditions, capturing their mechanical

Table 3
Geometrical and physical properties of novel and straight steel fibers.

Parameter	fiber length	fiber diameter (d_f)	Spherical end diameter (d_e)	Aspect ratio	f_{ft}	E_f
Spherical-End	30 mm	0.4 mm	0.6 mm	50	1180 MPa	210 GPa
Straight	30 mm	0.4 mm	0.0 mm	50	1180 MPa	210 GPa

behavior more accurately during extreme loading scenarios.

3.3. Traction–separation rule between fiber and matrix

In this study, a linear elastic bi-directional uncoupled traction-separation interaction was used to model the cohesive bond between the fibers and the cementitious matrix. This elastic response is described by a linear constitutive formulation in Eq. (5), which relates the traction stress tensor (t) and the equivalent slip displacements (δ) through the elastic stiffness matrix (K). This elastic model was defined for two effective directions: the normal axis (n) and the shear axis (s).

$$t = \begin{Bmatrix} t_n \\ t_s \end{Bmatrix} = \begin{bmatrix} k_{nn} & 0 \\ 0 & k_{ss} \end{bmatrix} \begin{Bmatrix} \delta_n \\ \delta_s \end{Bmatrix} = K\delta \tag{5}$$

The traction-separation curve can be divided into three parts: linear elastic, linear softening, and debonding. In Fig. 8, δ_c is the critical separation distance, τ_{max} is the interfacial strength, and δ_f is the failure separation distance. Also, G_c is the area under the traction-separation curve, representing the separation fracture energy.

Based on Fig. 8, the following relationship can be presented for the interfacial behavior:

$$\tau = \begin{cases} \tau_{s0}(\delta/\delta_{s0}) & 0 \le \delta \le \delta_{s0} \\ \tau_{s0}\dfrac{(\delta_{sf}/\delta)}{\tau_{s0}(\delta_{sf}/\delta_{s0})} & \delta_{s0} \le \delta \le \delta_{sf} \\ 0 & \delta_{sf} < \delta \end{cases} \tag{6}$$

With the three parameters τ_{s0}, δ_{s0}, and δ_{sf} the cohesive behavior of the fibers with the cementitious matrix can be defined.

The traction–separation rule parameters for the fiber-matrix interface, including τ_{s0}, δ_{s0}, and δ_{sf}, were estimated using the methodology depicted in Fig. 9. To predict these parameters for the novel spherical-end fibers, data from pull-out tests of straight fibers without spherical ends were employed. An embedment depth of L_e= 20 mm, consistent with the experimental setup, was considered. The estimation process relied on the inverse finite element method, initially introduced by Liu et al. [48], to predict mechanical properties such as elastic modulus and viscosity. The method, as illustrated in Fig. 9, utilizes optimization techniques to minimize the Root Mean Square (RMS) error between the numerical simulation results and the experimental data. This approach ensures accurate prediction of the traction–separation rule parameters for the fiber-matrix interface [49–51].

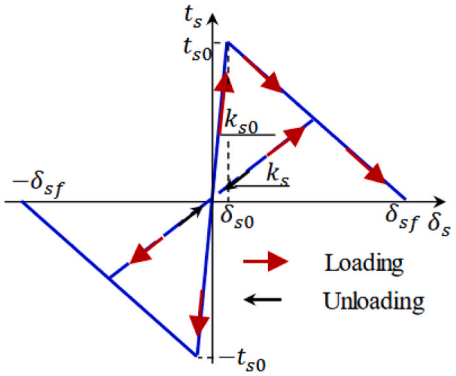

Fig. 8. Traction-separation law [47].

In the iterative process, based on the results of reference [52], the initial values for the three parameters, τ_{s0}, δ_{s0}, and δ_{sf}, are set to 2.8×10^{-3} mm, 8.23 MPa, and 12.8×10^{-3} mm, respectively. In each iteration, the Root Mean Square (RMS) error of the pull-out force between the finite element model and the experimental results is calculated. The iterative process is stopped when the RMS error falls below 2 %. In this study, after 98 iterations, the optimization process estimates the parameters τ_{s0}, δ_{s0}, and δ_{sf} as shown in Table 4.

3.4. Fiber pull-out simulation

The pull-out performance of the novel spherical-end steel fibers from UHPC reinforced with 1 wt% zirconium oxide nanoparticles was investigated using ABAQUS software. The simulation focused on analyzing the force-displacement relationship and the energy absorbed during the pull-out process. Fig. 10 illustrates the geometric model used for the fiber pull-out simulation, where the steel fiber is embedded in a cylindrical concrete matrix. The components of the pull-out model include the concrete matrix, the steel fiber, and the fiber-matrix interface. Consistent with the experimental setup, loading was applied as displacement control at a rate of 0.05 mm/min to the outer end of the fiber, while the bottom end of the concrete matrix was fully constrained. For the finite element analyses, a nonlinear dynamic solution method was employed, incorporating the effects of geometric nonlinearities to ensure accurate representation of the pull-out behavior.

In this study, three-dimensional solid elements (C3D20R) were employed for meshing both the concrete matrix and the steel fiber, as depicted in Fig. 11a. A mesh sensitivity analysis was conducted to determine the optimal element size, with the results summarized in Fig. 11b. The sensitivity analysis plots the pull-out force against the number of elements. It was observed that as the number of elements increased, the pull-out force converged to a specific value. Beyond 560,000 elements, the results showed negligible variation, indicating that further refinement would not significantly impact the accuracy of the model. Consequently, this element count was adopted for meshing the finite element models in this study.

3.5. Three-point bending simulation

The three-point bending test of an UHPC fiber-reinforced concrete beam, enhanced with 1 wt% zirconium oxide nanoparticles, was simulated using ABAQUS software. The simulated beam dimensions and geometric specifications were identical to those used in laboratory experiments for determining flexural strength.

The model included a three-dimensional UHPFRC beam and three rigid bodies representing the hydraulic jack and the supports. The concrete matrix was modeled using the CDP model, which accounts for the distinct tensile and compressive behavior of the concrete. A dynamic solution method was employed for the finite element analyses, incorporating geometric nonlinearities to accurately capture the beam's response under loading. A surface-to-surface contact interaction was defined to simulate the contact between the beam and the rigid bodies, with appropriate contact properties specified. A simple support boundary condition was applied at both ends of the beam, while a displacement boundary condition was imposed on the two rigid bodies to simulate the loading conditions.

As previously mentioned, another innovation of this work is the use of a multiscale finite element method to investigate the mechanical behavior of UHPC reinforced with novel spherical-end fibers. In this

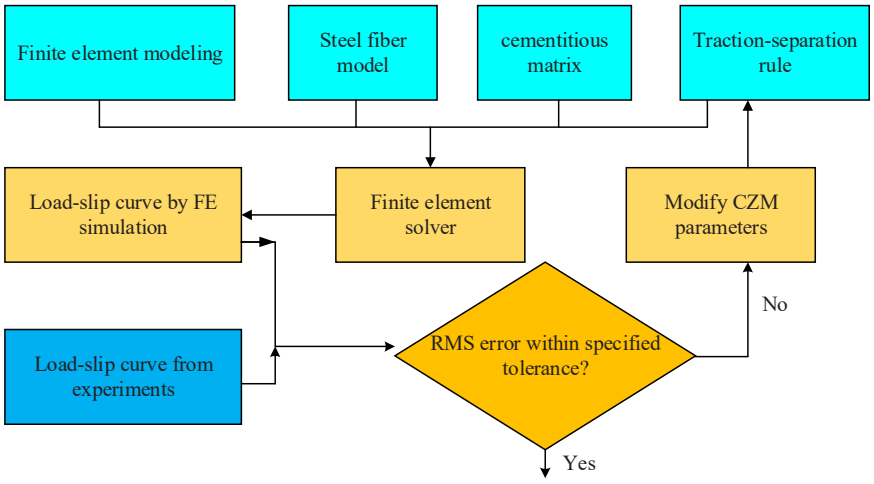

Fig. 9. Inverse finite element method based on optimization techniques for estimating traction–separation rule parameters between fiber and cementitious matrix.

Table 4
Parameters of the cohesive zone model for defining the interaction between steel fibers and cementitious composite.

	t_c	δ_c	δ_f
Steel fiber	20.15 MPa	2.1×10^{-3} mm	0.25 mm

approach, three-dimensional geometric models are created where individual fibers are placed discretely with varying distributions and random orientations. Unlike previous studies, this research incorporates the effects of fiber orientation and quantity by positioning the fibers randomly and irregularly to simulate the realistic conditions of fiber distribution within the ultra-high-performance concrete. To create the three-dimensional geometric model of randomly distributed fibers within the matrix, a program was written in MATLAB, and the scripting environment of ABAQUS was also used. In the three-dimensional model, the fibers are generated within the matrix as cylindrical bodies, consistent with their geometric shape. In the MATLAB program, the coordinates of a point at the corner of one fiber are first generated using a random function, considering the dimensions and angles relative to the coordinate axes. Then, to create another point on the fiber, the program checks to ensure that the fiber does not intersect with adjacent fibers. If no intersection occurs, the main axis of the fiber passes through these two points, thus establishing the random orientation of the fiber in space. If an intersection is detected, the program selects another point. The intersection check is repeated until the desired number of points (one point at the corner of each fiber) is created. Finally, the coordinates of a specific point on each fiber and their orientation angles relative to the coordinate axes are saved as output in a data file. This data file is then imported into the scripting environment of ABAQUS to generate the geometric modeling of the fibers with a random distribution in three dimensions. In this type of modeling, the load is transferred from the fibers to the matrix, and then the transfer of force and displacement occurs between the matrix and the fibers. Based on this, the mechanical behavior of fiber-reinforced concrete can be studied. The code written allows for the geometric modeling of fiber-reinforced UHPC using the multiscale model by accepting user-defined inputs such as the geometric dimensions of the fibers, Young's modulus, Poisson's ratio, yield stress, and the desired volume fraction. This also incorporates meshing and the

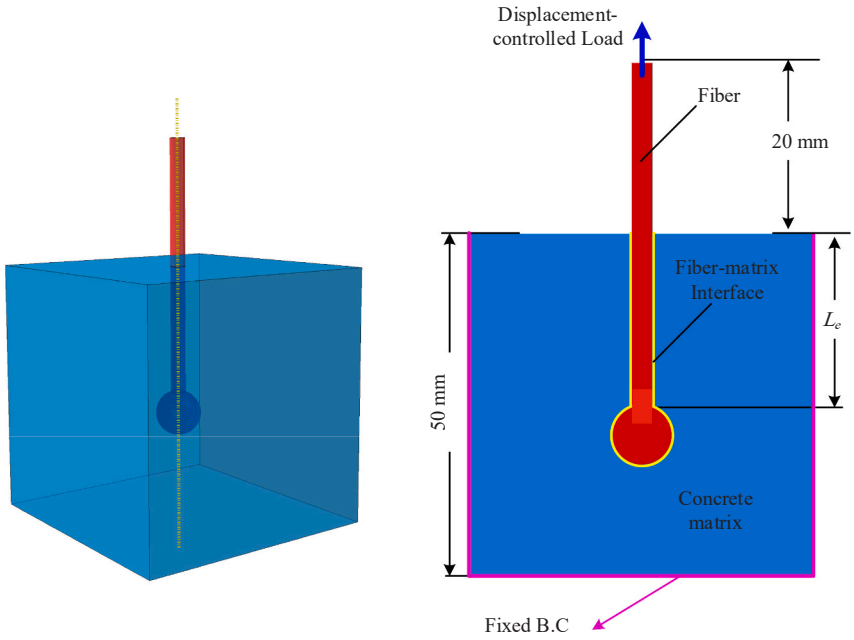

Fig. 10. Geometric model of fiber pull-out simulation showing concrete matrix, novel steel fiber, and fiber-matrix interface.

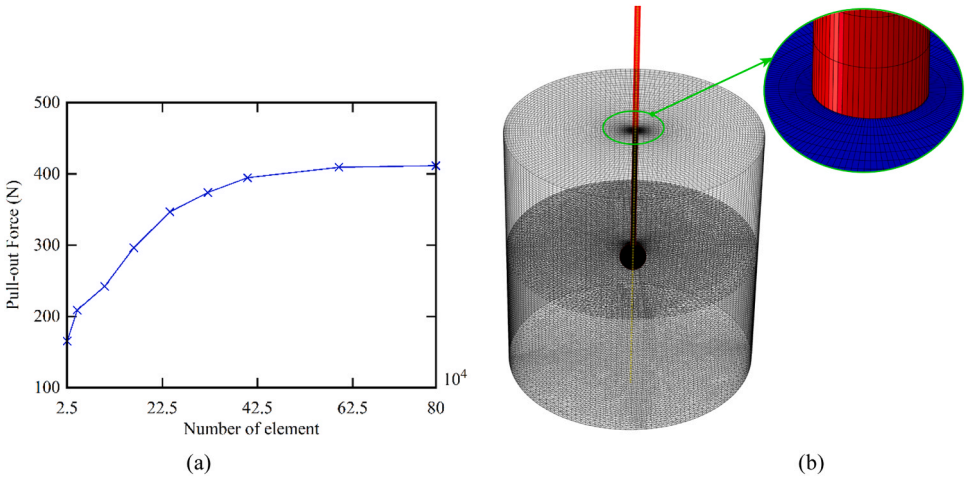

Fig. 11. (a) finite element model of fiber pull-out; (b) mesh sensitivity analysis showing pull-out force convergence with increasing number of elements.

application of boundary conditions and interactions.

To simulate damage and debonding phenomena at the fiber-concrete interface, the CZM theory (as described in Section 3.3) was employed, utilizing force-displacement diagrams. The parameters of these diagrams, used in the finite element model, were obtained by calibrating the numerical results with corresponding experimental data. Fig. 12 presents examples of geometric models featuring random fiber distributions generated using the algorithm outlined in the preceding section. These models correspond to a 2 wt% fiber volume fraction. The three-dimensional geometry permits fibers to have varying orientations, lengths, and spatial positions. Fig. 12b, c, and d depict fiber positions in the *xy*-plane, showcasing the effectiveness of the algorithm in producing a realistic distribution of fibers within the concrete matrix. This randomized distribution closely replicates the experimental fiber arrangement, providing a reliable basis for accurately predicting experimental outcomes.

After constructing the geometric model of fibers with varying volume fractions and sizes, the fibers were embedded within the UHPC matrix. Cohesive conditions were applied at the interfaces between the fibers and the UHPC matrix, and appropriate boundary conditions and loading were defined to assess the flexural strength behavior of the UHPC, reinforced with 1 wt% zirconium oxide nanoparticles and spherical-end steel fibers. Due to the geometric complexity of the structure, nonlinear 20-node hexahedral C3D20R elements were used to mesh the fibers, while nonlinear 10-node tetrahedral C3D10 elements were employed to mesh the three-dimensional matrix models. A dynamic load was then applied to the models to investigate the influence of various parameters, such as the geometric and mechanical properties of the fibers, their volume fraction, and their impact on the flexural strength of the material. The boundary conditions and interactions

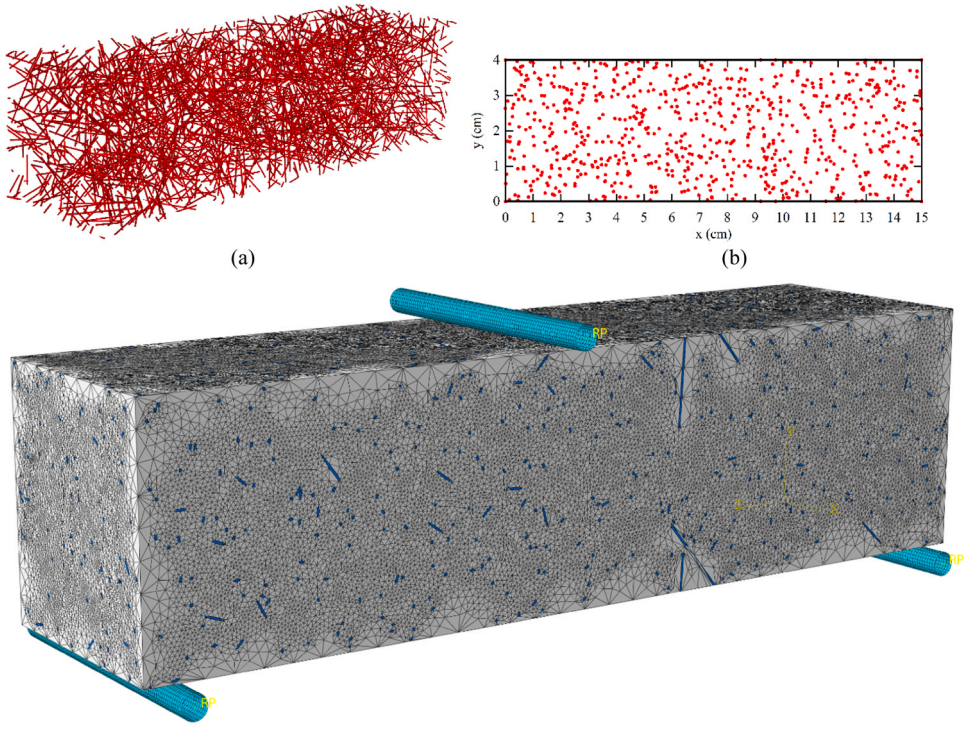

Fig. 12. Geometric models of random fiber distributions: (a) 3D fiber distribution; (b) fiber positions in the *xy*-plane; (c) Meshed model of three-point bending test.

between the fibers and the concrete matrix were precisely defined. For the analysis, a nonlinear dynamic method was used, and the simulation results were validated by comparing them with available experimental data.

4. Results

4.1. Influence of zirconium oxide nanoparticle content on mechanical properties of concrete

The average compressive strength results for three specimens are presented in Table 5. Fig. 13 illustrates the variation in compressive strength as a function of zirconium oxide nanoparticle substitution. The results indicate that the incorporation of zirconium oxide nanoparticles leads to an increase in compressive strength. Specifically, for concrete specimens containing 1 wt% zirconium oxide nanoparticles, the compressive strength increased by 44 % at 7 days and 37 % at 28 days. This improvement can be attributed to the influence of zirconium oxide nanoparticles on cement hydration, accelerating the cement hydration process. Another contributing factor is the high stability and uniform distribution of the nanoparticles, which enhance the mechanical properties of UHPC.

Fig. 14 presents scanning electron microscope (SEM) images, showing the uniform distribution of nanoparticles within the concrete matrix. The increase in compressive strength is further due to filling properties of nanoparticles and their role in connecting and bridging microcracks. SEM images from fractured surfaces of concrete specimens containing 0.5 wt% nanoparticles demonstrate that ultrasonic waves effectively dispersed the nanoparticles within the concrete mix. Additionally, while both plain concrete and concrete reinforced with 0.5 wt % zirconium oxide nanoparticles contain small pores, fewer defects are visible in specimens with 1 wt% zirconium oxide nanoparticles. Based on the improved microstructure and compressive strength, concrete modified with 1 wt% zirconium oxide nanoparticles is considered optimal for enhancing mechanical performance.

The average tensile strength measurements for three specimens are presented in Table 6. Fig. 15 illustrates the variation in tensile strength as a function of zirconium oxide nanoparticle substitution. The results indicate that the tensile strength increases with the addition of nanoparticles up to 1 wt%, after which it begins to decrease. Initially, the tensile strength remains relatively constant with the incorporation of nanoparticles but decreases with higher nanoparticle content. This reduction in tensile strength can be attributed to the agglomeration and clustering of nanoparticles at higher weight percentages. Due to their higher surface adhesion forces, zirconium oxide nanoparticles tend to agglomerate more at elevated concentrations, which may hinder their beneficial effects. The tensile strength of concrete specimens containing 1 wt% zirconium oxide nanoparticles increased by 62 % at 7 days and 38 % at 28 days. This indicates that the increase in tensile strength is more pronounced at younger ages, reflecting the accelerated hardening of the cement paste and the enhanced early setting of the concrete. Even in the worst-case scenario, where 0.5 wt% nanoparticles are added, the tensile strength improved by approximately 12 %. This enhancement can be attributed to the large specific surface area of zirconium oxide

Table 5
Compressive strength results of plain concrete specimens.

Mix ID	7-Day Compressive Strength (MPa)	28-Day Compressive Strength (MPa)
Control	36	86
0.5 % ZrO2	41	98
1.0 % ZrO2	52	118
1.5 % ZrO2	50	115

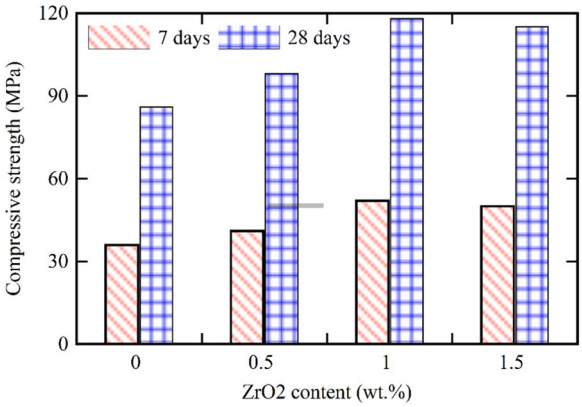

Fig. 13. Compressive strength of plain UHPC and UHPC containing zirconium oxide nanoparticles.

nanoparticles, which improves the bond between the concrete components and inhibits the growth of microcracks within the matrix.

The efficiency of zirconium oxide nanoparticles in enhancing tensile strength was approximately 62 %, which can be attributed to the surface effects of the nanoparticles. These surface effects react more rapidly than the cement itself, influencing tensile strength at both early and later ages. The spherical shape and rough texture of ZrO_2 nanoparticles enable greater bonding between the aggregate particles and the cement paste, which results in increased adhesion strength and consequently enhanced tensile strength [53]. Moreover, previous studies have reported a phase transformation in ZrO_2, where zirconia in the tetragonal phase undergoes a martensitic transformation to the monoclinic phase under mechanical stress. This transformation involves an approximate 4 % increase in volume, which could contribute to the inhibition of crack propagation and further enhancement of tensile strength [54]. However, more research is needed to fully understand and isolate this reinforcement mechanism within the cementitious matrix. Additionally, the ZrO_2 nanoparticles, due to their greater surface area, increase the packing density of cement particles, reducing the volume of permeable pores within the concrete mixture [55]. This effect is known as the "filler effect," where ZrO_2 particles fill the voids or pores created during cement hydration, enhancing the material's overall strength. The "nucleation effect" is another reinforcement mechanism, where ZrO_2 particles serve as preferential nucleation sites for cement hydration products [56]. This leads to the formation of a higher content of C-S-H tobermorite phase and inhibits the growth of calcium hydroxide ($Ca(OH)_2$) crystals, further strengthening the matrix.

4.2. Validation of results

The validation of the FE model for fiber pull-out was conducted by comparing the simulation results with experimental test results for spherical-end steel fibers and straight steel fibers, as shown in Fig. 16. The experimental tests were performed on concrete containing 1 wt% zirconium oxide nanoparticles, with fiber parameters of l_e= 10 mm, d_f= 0.4 mm, and d_e= 0.6 mm. The comparison shows that the FE model accurately matches the linear elastic portion of the pull-out curve. However, a slight deviation occurs after debonding, which is expected due to the complexities in modeling the mechanical behavior of cementitious composites and fibers. The error in estimating the pull-out force and fracture energy for the straight steel fibers was found to be 3.8 % and 2.9 %, respectively—both of which are considered acceptable. These low errors are attributed to the careful calibration between numerical and experimental results. Following the calibration of the traction-separation rule parameters using the results for straight steel fibers, the model's results for the spherical-end fibers were validated. The maximum pull-out force for the spherical-end fibers in the

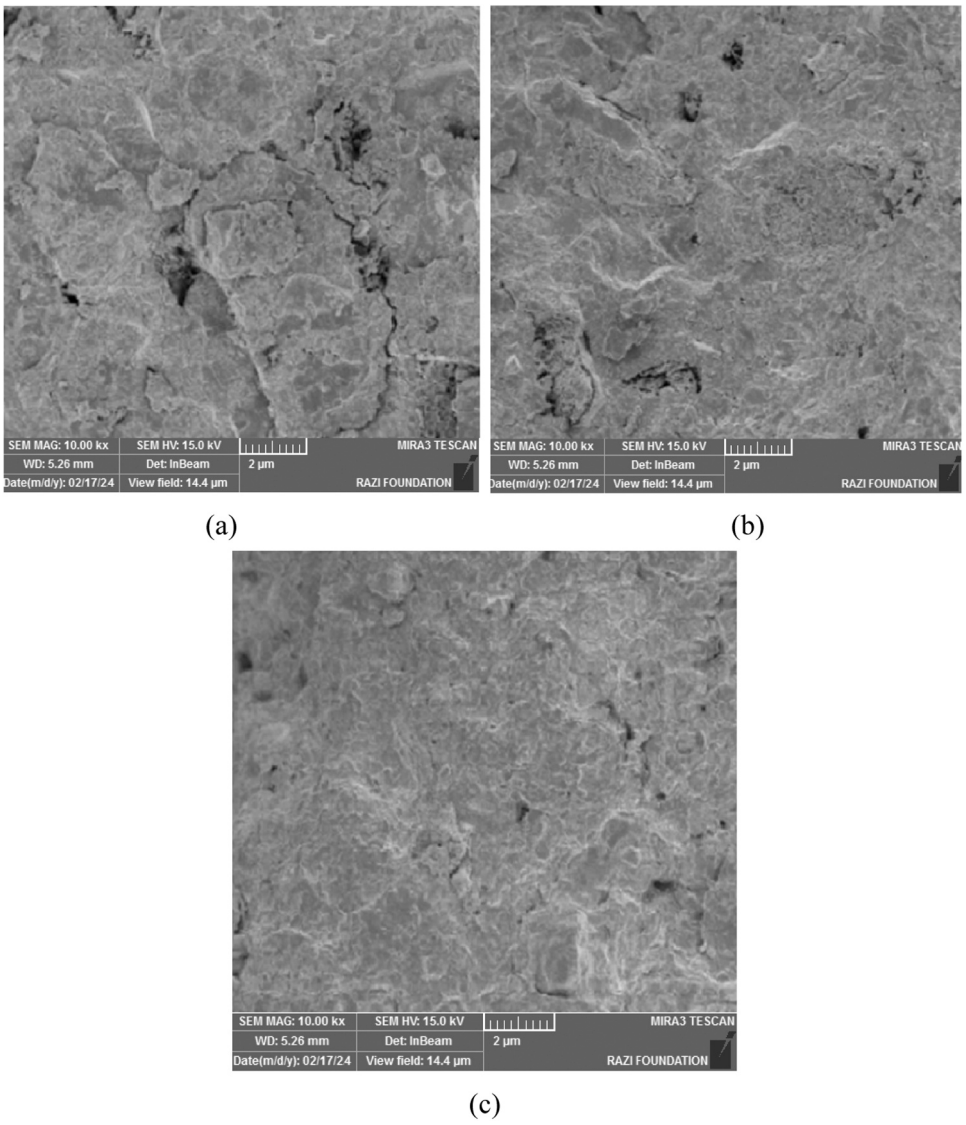

Fig. 14. SEM images of fractured surfaces of compressive concrete specimens containing different amounts of zirconium oxide nanoparticles: (a) 0 wt%, (b) 0.5 wt%, and (c) 1 wt%.

Table 6
Tensile strength results of plain UHPC specimens.

Mix ID	7-Day Tensile Strength (MPa)	28-Day Tensile Strength (MPa)
Control	1.38	2.86
0.5 % ZrO2	1.93	3.24
1.0 % ZrO2	2.23	3.97
1.5 % ZrO2	2.07	3.70

numerical model was 210.5 N, compared to 215.8 N in the experimental results, resulting in a 3.3 % error. The absorbed energy in the numerical model was 4.23 N.m, while the experimental results showed 3.88 N.m, yielding a 12 % error. A key observation from the comparison between the novel spherical-end steel fibers and straight steel fibers is the significant improvement in the performance of the spherical-end fibers. Specifically, the pull-out force increased by 124 %, and the pull-out energy improved by 188 %, demonstrating the superior mechanical behavior of the spherical-end design.

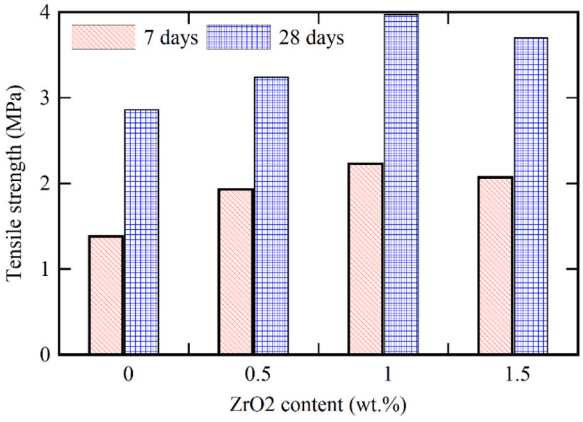

Fig. 15. Tensile strength of plain UHPC and UHPC containing zirconium oxide nanoparticles.

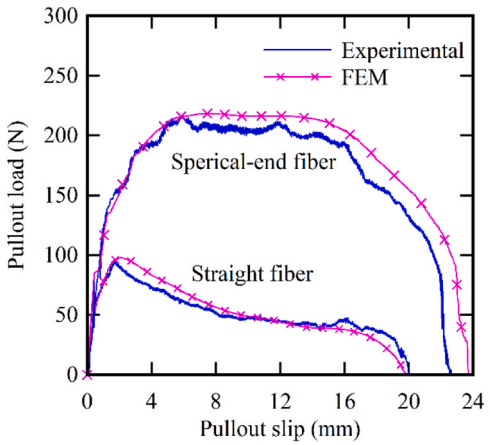

Fig. 16. Comparison of pull-out force versus slip for straight and spherical-end (d_e=0.6 mm) steel fibers (both with fiber diameter d_f = 0.4 mm, embedded length l_e = 10 mm, and high-carbon steel material).

4.3. Investigation of the effect of fiber geometric parameters

The presence of spherical ends on steel fibers significantly affects their pull-out behavior compared to straight fibers, as observed in the results presented in Fig. 17. The pull-out response of straight steel fibers with a diameter of d_f= 0.5 mm is shown, highlighting the differences in the resistive forces involved. For straight fibers, the pull-out resistance consists of two primary components: bond resistance and frictional resistance. As seen in Fig. 17a, the curve exhibits a sudden drop after reaching the maximum force (point C), which corresponds to a sharp reduction in bond resistance. Beyond point D, the only remaining resistive force is the frictional force, which continues to oppose the fiber's pull-out but at a reduced level compared to the bond resistance phase. The stress distribution at various marked positions along the pull-out curve is provided in Fig. 17b, which helps to further elucidate how the forces evolve as the fiber is pulled out of the matrix. This behavior is typical for straight fibers, where the bond between the fiber and the matrix plays a dominant role in resisting pull-out until failure occurs, after which friction becomes the primary resistive force.

In contrast, the behavior of spherical-end fibers is completely different. Fig. 18 shows the pull-out response of spherical-end steel fibers. In Region 1, there is bond resistance that is completely lost at point A. After this point, the debonding process begins from the outer part of the fiber. Subsequently, mechanical interlocking becomes the main resistance factor against pull-out. In this region, from point A to points B and C, the embedment of the spherical end of the fiber in the concrete creates an effective barrier against pull-out and causes significant tensile strain to develop in the fiber. Ultimately, the drop in bond resistance of the fiber can result from two factors: either the rupture of the fiber or the fiber being pulled out of the concrete due to the degradation of the concrete surrounding the spherical end of the fiber. After the mechanical interlocking of the fiber with the concrete matrix is lost, the fiber is easily pulled out of the concrete, and the only resistive force is the frictional force. As shown in Fig. 18b, for d_e= 0.7 mm, the spherical end of the fiber causes the concrete to be pulled out, and the failure mode is that of fiber pull-out.

Fig. 19 shows the pull-out failure mode of spherical-end steel fibers with a diameter of d_e= 0.7 mm. As shown, with an increase in the diameter of the spherical end of the fibers, minor failure occurs in the upper part of the fiber-concrete interface. In this case, due to the high contact area of mechanical interlocking, the concrete is not pulled out, and the failure occurs as fiber rupture. Unlike conventional fibers that separate at the interface with the matrix, in the spherical-end fibers, failure often occurs as a rupture within the fiber itself, which indicates that the full tensile capacity of the fibers is being utilized.

4.4. Pull-out force-slip responses

Fig. 20 illustrates the influence of the geometric parameters of fiber ends, namely the fiber diameter d_f and the end diameter d_e, on the force-slip curve for fibers with an embedment length L_e= 20 mm. The pull-out performance of straight fibers and spherical-end fibers is examined, and several key observations can be made. For straight fibers, the slip behavior leads to a slip-type failure, where the fiber slides out of the matrix as it is pulled. In contrast, spherical-end fibers exhibit an additional mechanism: mechanical interlocking between the matrix and the end of the fiber. This interlocking, in addition to the usual chemical bonding and frictional resistance, increases the bond strength and resistance to pull-out. Specifically, the mechanical interlocking between the spherical end of the fiber and the cementitious composite contributes significantly to the overall bond strength, which results in a higher bond stress and enhances the fiber's pull-out resistance. This behavior is particularly important because it allows the fiber to resist greater stresses before rupture occurs, making full use of the fiber's maximum tensile capacity.

The configuration with d_e= 0 and d_f= 0.4 mm is representative of a typical smooth straight steel fiber, commonly used in UHPC applications. This fiber has no anchorage or deformation at the ends, leading to bond-dominated pull-out behavior. Its dimensions are in line with standard commercially available straight fibers, making it an appropriate reference for evaluating the enhancement provided by the spherical-end design. The geometric parameters, such as d_f and d_e, play a crucial role in determining the efficiency of this bonding mechanism. For instance, increasing the fiber diameter d_f leads to a higher maximum

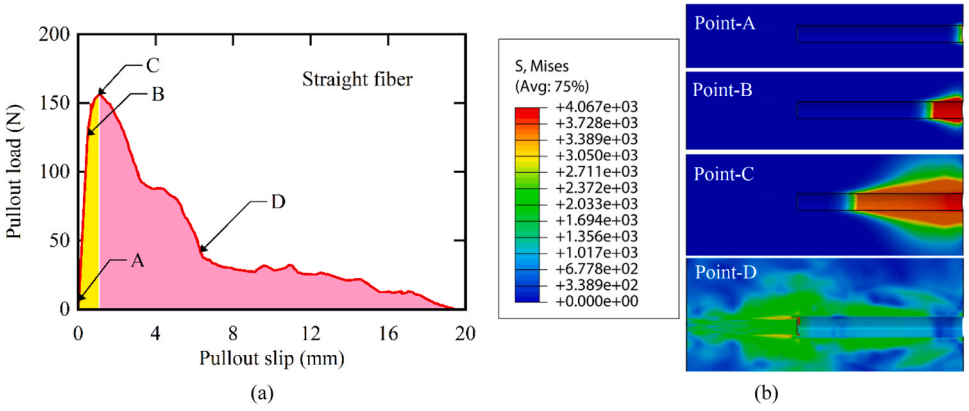

Fig. 17. (a) Pull-out response of straight steel fibers from concrete reinforced with 1 wt% zirconium oxide nanoparticles and (b) stress distribution at various locations during the pull-out process.

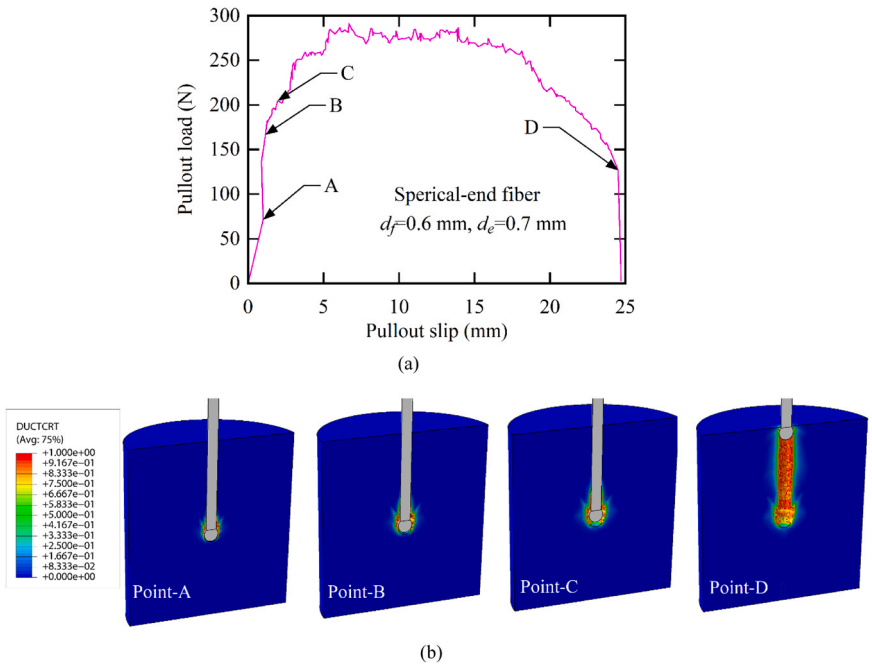

Fig. 18. (a) Pull-out response of spherical-end steel fibers from concrete reinforced with 1 wt% zirconium oxide nanoparticles, and (b) stress distribution at various locations during the pull-out process.

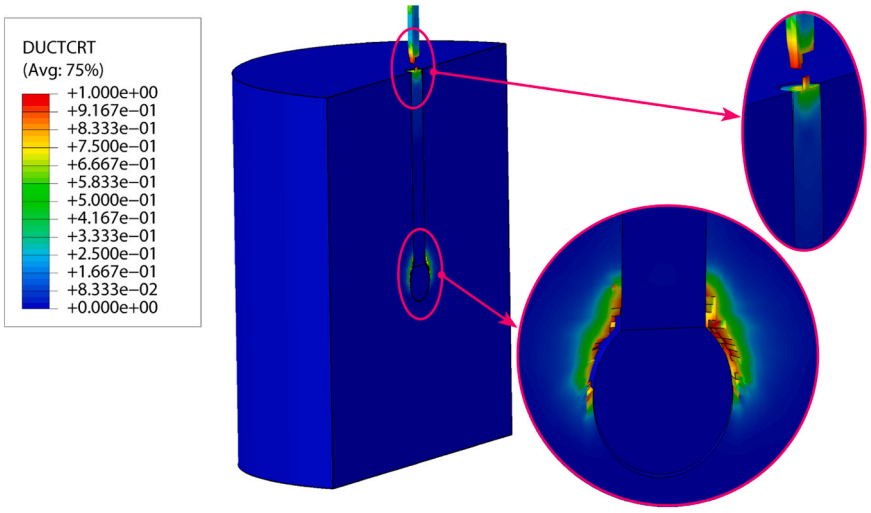

Fig. 19. Pull-out failure mode of spherical-end steel fibers with a diameter of d_e= 0.7 mm.

pull-out force, as a larger fiber diameter creates more mechanical interlocking between the fiber and the matrix. Similarly, varying the end diameter d_e influences the pull-out behavior. For small values of d_e, the pull-out is predominantly slip-type. However, as d_e increases, up to a certain threshold, the pull-out behavior shifts toward a combination of slip-type failure and fiber rupture, where the fiber undergoes fracture due to the tensile stresses it endures. This transition enhances the fiber's overall performance by utilizing the maximum tensile strength of the fiber. In summary, the pull-out force increases with both d_f and d_e, with the most significant effect coming from the mechanical interlocking of the fiber end with the cementitious composite, which enhances the bond strength and leads to greater pull-out resistance.

Based on the force-slip curves in Fig. 20, the key parameters of these curves, including the maximum pull-out force (P_{max}), the slip value corresponding to the maximum force (δ_{max}), the area under the pull-out curve (pull-out energy, G), and the bond stress (τ), are presented in Table 7.

$$\tau_{\max} = \frac{P_{\max}}{\pi d_f L_e} \tag{7}$$

in which P_{max} is the maximum pull-out force, d_f is fiber diameter, and le is embedment length of fiber.

The results of the study highlight significant improvements in the pull-out behavior of the newly presented spherical-end fibers compared to straight fibers. Specifically, the pull-out force and total pull-out energy (the area under the force-slip curve) increase with both the fiber diameter (d_f) and the end diameter (d_e). For fibers with a diameter of 0.4 mm, an increase in d_e from 0 to 0.7 mm results in a dramatic increase in both the pull-out force and pull-out energy, with gains of approximately 300 % and 277 %, respectively. However, the maximum pull-out energy and displacement corresponding to the pull-out force occur at d_e= 0.6 mm. Any further increase in d_e beyond this value tends to

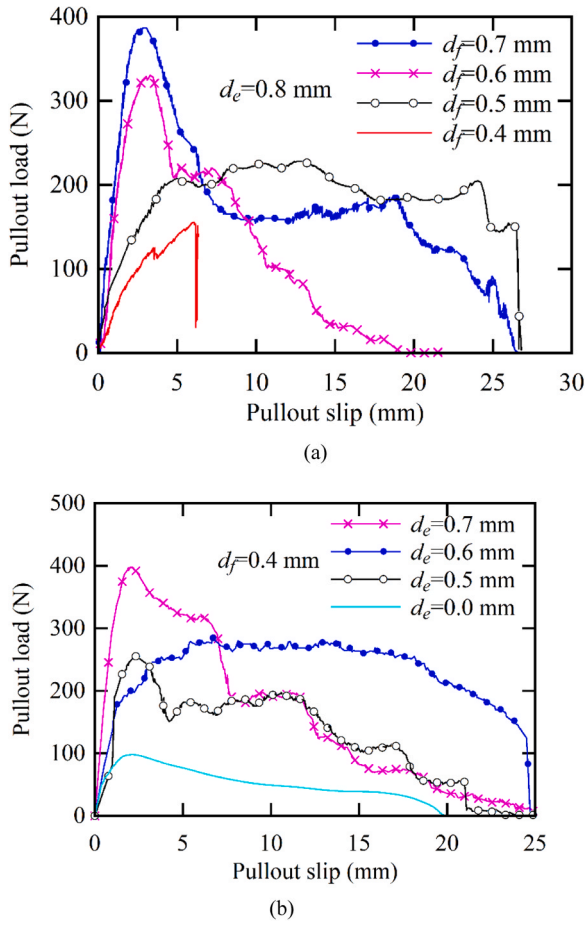

Fig. 20. Influence of geometric parameters of the fiber end on the force-slip curve: (a) variation with fiber diameter d_f, and (b) variation with end diameter d_e. The case of d_e= 0, d_f= 0.4 mm corresponds to a conventional straight steel fiber and is used as the reference case.

negatively affect the pull-out energy. This indicates that there is an optimal size for d_e beyond which the performance begins to deteriorate.

The newly presented fibers consistently outperform straight fibers in terms of pull-out energy, with a worst-case scenario showing a 110 % improvement in energy. This suggests that spherical-end fibers significantly enhance the pull-out performance from the cementitious composite. The bond stress for straight fibers is 3.89 MPa, while the bond stress for spherical-end fibers increases up to 15.82 MPa, reflecting a 3.06-fold increase in bond strength. This increased bond stress is a key factor in the enhanced pull-out behavior of spherical-end fibers.

Regarding failure modes, spherical-end fibers demonstrate a pull-out failure mode, primarily due to the degradation of the concrete around the fiber tip, which results in high pull-out energy. In contrast, when fiber rupture occurs, the maximum tensile capacity of the fibers is fully utilized. The applied stress exceeds the tensile strength of the fiber during the pull-out process, leading to fiber rupture. This behavior indicates that the best performance for spherical-end fibers is achieved when fiber rupture occurs, confirming that the fibers are effectively utilizing their maximum tensile strength during the pull-out process.

Although an overall trend indicates that increasing d_f or de leads to improved pull-out resistance and higher bond stress, the failure modes in Table 7 do not follow a strictly progressive pattern. Specifically, fiber rupture does not consistently occur with increasing end diameter (d_e) or fiber diameter (d_f); instead, pull-out failure reappears at certain combinations, particularly at intermediate aspect ratios of d_e/d_f. This selective failure behavior can be attributed to a complex interplay of the following mechanisms:

1. Stress redistribution at the fiber tip: For certain d_e/d_f ratios, the spherical end creates localized stress concentrations in the surrounding matrix. If the matrix around the enlarged tip is unable to resist these stresses due to insufficient confinement or microcracking, the concrete fails before the fiber reaches its tensile limit, leading to pull-out rather than rupture.
2. Anchorage efficiency versus local matrix damage: As de increases, mechanical interlocking improves, but so does the risk of concrete cone failure around the fiber tip. At certain d_e/d_f thresholds, the pull-out force becomes high enough to cause local matrix spalling, which in turn reduces the effectiveness of the anchorage and results in pull-out.
3. Geometric threshold for rupture: Full utilization of the fiber's tensile capacity—and thus rupture—only occurs when anchorage is sufficient and the applied stress is transferred effectively along the fiber's embedded length without inducing premature matrix failure. This balance is disrupted at certain aspect ratios, explaining why rupture is not always observed even when bond stress is high.

These results suggest that the failure mode is not solely a function of increasing d_f or de, but rather depends on the combined geometry, local matrix integrity, and load transfer mechanisms. This insight is critical for optimizing the geometry of spherical-end fibers to ensure consistent tensile failure, which maximizes energy absorption.

4.5. *Three-point bending loading*

The three-point bending test was performed on an UHPC specimen containing 1 wt% steel fibers and 1 wt% zirconium oxide nanoparticles. Fig. 21 shows the failure pattern of the fiber-reinforced UHPC specimen under flexural loading. In specimens containing fibers, after the formation of a crack, the fibers in the UHPC prevent its propagation and, by bridging the two sides of the crack, delay its growth and increase the flexural strength or toughness of the concrete. Furthermore, the results show that the presented multiscale FE model accurately estimates the failure behavior in this specimen. The load-displacement curves obtained from the FE model and the flexural strength test for the UHPC specimen containing 1 wt% steel fibers and the plain specimen are presented in Fig. 22. As shown, there is good agreement between the

Table 7
Pull-Out force and energy comparison for straight and spherical-end steel fibers.

No	d_e (mm)	d_f (mm)	d_e/d_f	Pull-out Force (N)	Critical Separation (mm)	Pull-out Work (N/mm)	Bond Stress (MPa)	Failure mode
1	0.8	0.4	2.00	155.5	6.06	0.93	6.19	Rupture of fiber
2		0.5	1.60	228.1	12.8	5.06	7.26	Pull-out
3		0.6	1.33	330.9	3.28	2.62	8.78	Rupture of fiber
4		0.7	1.14	386.5	2.82	4.69	8.79	Rupture of fiber
5	0.0	0.4	0.00	97.0	2.08	1.06	3.86	Pull-out
6	0.5		1.25	256.9	2.24	3.08	10.23	Rupture of fiber
7	0.6		1.50	285.4	6.60	5.37	11.36	Pull-out
8	0.7		1.75	397.3	2.07	3.99	15.82	Rupture of fiber
9	Straight fiber	-	-	97.7	2.07	1.06	3.89	Pull-out

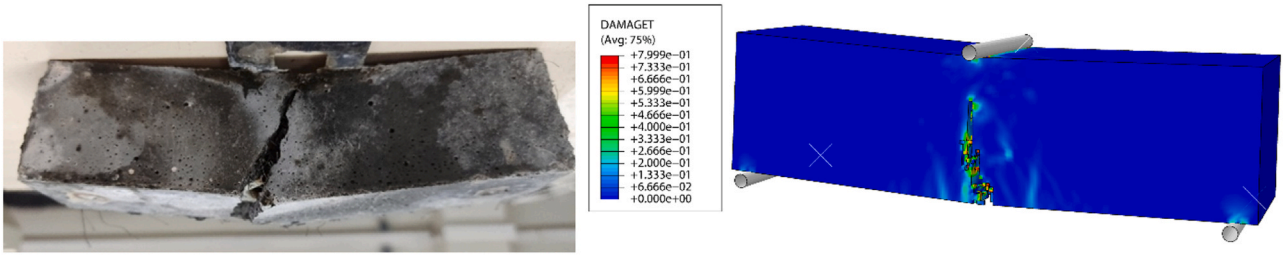

Fig. 21. Results of multiscale FE model and the experimental method showing the failure pattern of fiber-reinforced UHPC specimens under flexural loading.

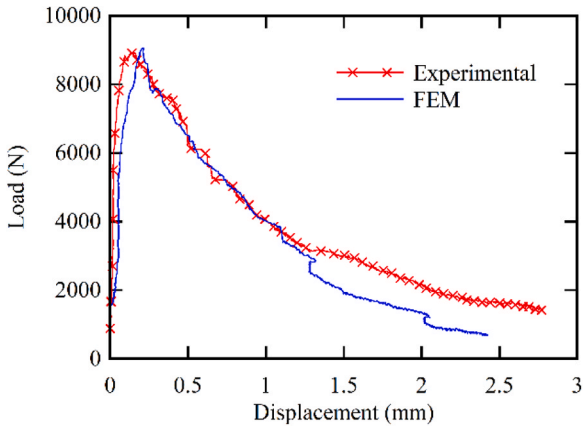

Fig. 22. Load-displacement curves obtained from the multiscale FE model and the flexural strength test for UHPC specimens reinforced with 1 wt% zirconium oxide nanoparticles and 1 wt% spherical-end steel fibers.

results of the laboratory specimen and the FE model.

To investigate the influence of the novel spherical-end fibers on the flexural behavior of UHPC, Fig. 23 shows the effect of the fiber volume fraction on the load-displacement curves obtained from the multiscale finite element model for UHPC containing the novel spherical-end fibers as well as straight steel fibers. The area under these curves represents the amount of energy absorption, or toughness. As expected, the addition of fibers increases the toughness. For the case of using 2 vol% fibers, the area under the load-displacement curve is approximately 27.91 N.m for the sample with novel spherical-end fibers, 27.21 N.m for samples with straight fibers and approximately 5.27 N.m for the unreinforced sample, which demonstrates the significant effect of the novel spherical-end fibers on the toughness of fiber-reinforced UHPC. Therefore, it can be concluded that, while the novel fibers significantly increase the flexural strength and toughness of UHPC. Also, according to the figure, it is observed that with an increase in the percentage of fibers in the ultra-high-performance concrete, a significant increase in flexural strength and, consequently, the maximum load that the beam samples can withstand, is observed. Furthermore, since the use of fibers increases the mid-span displacement of the beam for the maximum force values, the ultra-high-performance concrete with the novel fibers will have greater ductility before fiber failure. Spherical-end steel fibers are an effective innovation in the mechanical reinforcement of UHPC. By improving pull-out behavior and optimally utilizing the steel capacity, these fibers can have a wide range of applications in advanced structures and critical civil engineering projects.

Table 8
Summary of load-displacement curve results, including the maximum load capacity in the three-point bending simulation, the corresponding displacement at maximum load, as well as the flexural strength and toughness obtained from the multiscale finite element model.

Fibres Content (%)	Fibres Type	Max. Load (kN)	Displacement at peak load (mm)	Energy absorption (N.m)	Flexural strength (MPa(
0	-	2.93	0.023	0.29	6.87
0.5	Spherical-end fibers	3.48	0.221	3.44	8.16
	Straight fibers	3.02	0.112	0.97	7.08
1.0	Spherical-end fibers	5.66	0.514	8.53	13.27
	Straight fibers	3.41	0.046	1.89	7.99
1.5	Spherical-end fibers	7.03	0.496	11.27	16.48
	Straight fibers	3.75	0.113	3.16	8.79
2.0	Spherical-end fibers	9.22	1.455	27.91	21.61
	Straight fibers	4.56	0.528	5.35	10.69

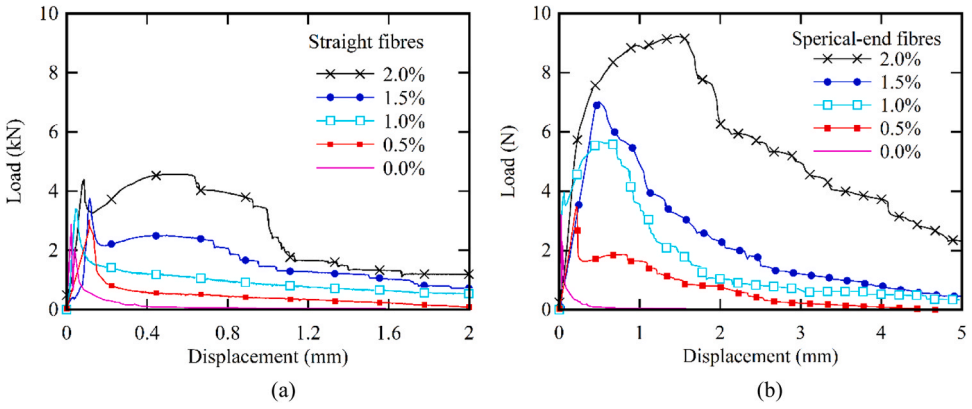

Fig. 23. Effect of fiber volume fraction on the load-displacement curves of ultra-high-performance concrete reinforced with 1 wt% zirconium oxide nanoparticles: (a) spherical-end steel fibers and (b) straight steel fibers.

Table 8 provides a comprehensive summary of the load-displacement curve results, including the maximum load capacity observed during the three-point bending simulation, the corresponding displacement at maximum load, as well as the flexural strength and toughness values derived from the multiscale finite element model for both straight steel fibers and spherical-end steel fibers. The results underscore the significant enhancement in concrete properties, particularly with respect to toughness and energy absorption capacity, which are pivotal in influencing the failure behavior of concrete. As evidenced in the table, the incorporation of spherical-end steel fibers notably improves the flexural strength of UHPC, with a 2.2-fold increase in flexural strength observed at a 2 vol% fiber volume fraction.

It is noteworthy that the effect of fiber addition on energy absorption capacity is more pronounced than its impact on other mechanical properties, particularly at lower fiber volume fractions. Specifically, at *a* 0.5 vol% fraction of spherical-end steel fibers, the energy absorption capacity increases by approximately 10.8 times compared to plain UHPC reinforced with straight steel fibers. Furthermore, the data in Table 8 reveals that, as the fiber volume fraction increases, the displacement corresponding to the maximum load also increases. The maximum increase in displacement, observed for the novel spherical-end fibers at 2 vol%, is 1.45 mm. Notably, the failure displacement for these fibers is increased by a factor of 62.3 compared to the plain concrete specimen. Additionally, the results highlight that the enhancement in energy absorption capacity and ductility due to increased fiber content is considerably more significant than the corresponding increase in concrete strength. With the addition of 2 vol% fibers, the flexural strength of concrete reinforced with spherical-end steel fibers is approximately 214 % greater than the plain specimen, whereas the increase for straight steel fibers is 55 %. The improved mechanical interlocking between the novel spherical-end fibers and the concrete matrix mitigates slippage and inhibits crack formation, thereby preserving the concrete integrity until the fibers themselves rupture. This interlocking mechanism is a key factor contributing to the enhanced flexural strength observed in UHPC reinforced with spherical-end fibers.

The significant strain hardening in the post-yield stage leads to the optimization of UHPC properties when reinforced with spherical-end steel fibers. This strain hardening results in a considerable increase in the energy dissipation area enclosed by the pull-out curves. Therefore, fiber bridging is an ideal method for improving strain hardening, and UHPC with spherical-end steel fibers may be well-suited for use in concrete structures subjected to earthquakes or shock loading, for dynamic energy absorption.

The results clearly demonstrate that UHPC specimens reinforced with spherical-end steel fibers exhibit significantly higher energy absorption capacity and ductility compared to those reinforced with conventional straight fibers. At a fiber volume fraction of 2.0 vol%, the energy absorption of specimens with spherical-end fibers reached 27.91 N.m, while that of straight fibers was limited to 5.35 N.m—representing a more than fivefold increase. Even at lower fiber contents (e.g., 0.5 vol%), the energy absorbed by spherical-end fiber-reinforced specimens (3.44 N.m) was over 3.5 times greater than that of straight fiber-reinforced specimens (0.97 N.m). This enhanced performance can be attributed to improved mechanical interlocking at the fiber-matrix interface and delayed fiber pull-out or rupture, resulting in a more extended post-cracking response. Furthermore, the displacement at peak load—a proxy for ductility—increased from 0.528 mm (straight fibers) to 1.455 mm (spherical-end fibers) at 2.0 vol%, indicating a 175 % improvement in deformability. These findings highlight the ability of spherical-end fibers to significantly improve the toughness and post-peak behavior of UHPC, making them particularly suitable for use in seismic, impact-resistant, or blast-exposed concrete structures where energy dissipation and crack control are critical.

5. Conclusion

In this study, the advantages of using novel spherical-end steel fibers in the reinforcement of cementitious composites were investigated using pull-out response analyses. To this end, the influence of the end geometry of the newly presented fibers on the pull-out performance of steel fibers was studied using experimental and FE methods. The interaction between the fibers and the cementitious composite was simulated using the concept of a cohesive zone interface, and its parameters were obtained using an inverse finite element method and the results of an experimental test performed on a single fiber specimen. After validating the results of the FE model with the results of the experimental examinations, the influence of the geometric parameters of the spherical ends of the fibers on the bonding characteristics of the fibers with the cementitious composite was studied. Based on the results presented, the following conclusions can be drawn:

This study has successfully demonstrated the significant advantages of utilizing novel spherical-end steel fibers in the reinforcement of cementitious composites, focusing on their impact on pull-out behavior and flexural performance. Through a combination of experimental testing and advanced finite element modeling, including a multi-scale approach, key findings have been established:

- **Enhanced Pull-Out Performance:** The incorporation of spherical ends on steel fibers results in a substantial improvement in pull-out performance compared to straight fibers. The spherical ends significantly enhance mechanical interlocking with the concrete matrix, leading to a 124 % increase in pull-out force and a 188 % increase in pull-out energy, thereby demonstrating a more efficient utilization of the fiber's tensile capacity.
- **Optimal Nanoparticle Content:** The addition of 1 wt% zirconium oxide nanoparticles to ultra-high-performance concrete (UHPC) results in the most favorable mechanical properties, with a 38 % increase in tensile strength and a 37 % increase in compressive strength. This is attributed to the nanoparticles' role in accelerating cement hydration and improving matrix homogeneity.
- **Influence of Fiber Geometry:** The geometric parameters of the spherical ends (*de*) significantly influence pull-out behavior. While increasing *de* enhances pull-out force and energy, an optimal value of $de = 0.6$ mm was identified for maximizing these properties. For *de* values greater than that, concrete pull-out occurs reducing the effectiveness of the spherical-end.
- **Multiscale Modeling Accuracy**: The developed multiscale finite element model accurately predicts the flexural behavior of UHPC reinforced with spherical-end fibers. The model demonstrates the enhanced energy absorption capacity and improved ductility associated with the use of spherical-end fibers when compared to straight fibers.
- **Superior Flexural Strength and Toughness:** The use of spherical-end steel fibers significantly improves the flexural strength and toughness of UHPC. In particular, at a fiber volume fraction of 2 vol %, the use of spherical-end fibers results in a 214 % increase in flexural strength when compared to plain UHPC.
- **Enhanced Energy Absorption:** The novel spherical-end fibers substantially increase the energy absorption capacity of UHPC. At low volume fractions, these fibers result in a significantly higher energy absorption capacity than that of conventional steel fibers at the same volume fraction.

In summary, this research highlights the potential of spherical-end steel fibers to act as a highly effective reinforcement in advanced cementitious materials. The superior pull-out characteristics of these fibers, coupled with enhanced mechanical interlocking, allow the full tensile capacity of steel to be utilized, translating to notable improvements in flexural strength and energy absorption capacity of UHPC. This study demonstrates the promise of spherical-end fibers for improving

the performance of structures subjected to various loading conditions, including flexural stresses, as well as, dynamic loads. The findings provide valuable insights for the development of more resilient and efficient concrete structures, particularly in critical civil engineering projects. Further research should focus on optimizing the fiber geometry and exploring other potential applications of this technology.

Future research can further develop the present numerical framework by validating the model under additional scenarios, such as alternative fiber geometries (e.g., hooked-end or hybrid fibers) and different loading conditions, including cyclic, dynamic, or impact loads. Extending the simulation model to account for long-term durability aspects—such as shrinkage, creep, and environmental degradation—would enhance the robustness and applicability of the findings for real-world conditions. Moreover, investigating the performance of spherical-end steel fibers in cementitious matrices with varying mechanical and physical properties, such as high-performance concrete (HPC), normal-strength concrete (NSC), and lightweight concrete (LWC), is strongly recommended. These materials differ significantly in terms of stiffness, density, and fracture behavior, which may affect the fiber-matrix bond mechanism and failure mode. Studying such variations could provide valuable insights into how matrix characteristics influence pull-out resistance, bond stress, and energy dissipation. These findings would support the optimization of fiber geometry for different matrix types and promote the broader application of spherical-end fibers across diverse structural and non-structural concrete systems.

CRediT authorship contribution statement

Hakan Çağlar: Writing – review & editing, Writing – original draft, Visualization, Methodology, Investigation, Data curation.

Declaration of Competing Interest

The authors declare that they have no known competing financial interests or personal relationships that could have appeared to influence the work reported in this paper.

Data availability

Data will be made available on request.

References

[1] I. Sharifi, M.H. Sherzai, A. Javanmard, F. Yalçındağ, İ.Ö. Yaman, An innovative method for Uniaxial tensile performance in the warp and weft directions of carbon textile reinforced concretes with two different matrices, Constr. Build. Mater. 476 (2025) 141292.

[2] J. Esmaeili, V. Romouzi, J. Kasaei, K. Andalibi, An investigation of durability and the mechanical properties of ultra-high performance concrete (UHPC) modified with economical graphene oxide nano-sheets, J. Build. Eng. 80 (2023) 107908.

[3] Y. Zheng, X. Lv, S. Hu, J. Zhuo, C. Wan, J. Liu, Mechanical properties and durability of steel fiber reinforced concrete: a review, J. Build. Eng. 82 (2024) 108025.

[4] S. Aidarov, A. Nogales, I. Reynvart, N. Tošić, A. de la Fuente, Effects of low temperatures on flexural strength of macro-synthetic fiber reinforced concrete: experimental and numerical investigation, Materials 15 (3) (2022) 1153.

[5] A.K. Pour, E. Noroozinejad Farsangi, Effect of polypropylene fibers on the bond-slip performance of HSS bars in HPC and UHPC, Adv. Struct. Eng. 27 (13) (2024) 2244–2270.

[6] S. Guler, Z.F. Akbulut, Residual strength and toughness properties of 3D, 4D and 5D steel fiber-reinforced concrete exposed to high temperatures, Constr. Build. Mater. 327 (2022) 126945.

[7] Ronanki, V.S., Hybrid structures using ultra high performance concrete and normal concrete for bridge applications. 2018: The University of Alabama.

[8] L. Rossi, M.P. Zappitelli, R.A. Patel, F. Dehn, Flexural tensile behaviour of alkali-activated slag-based concrete and Portland cement-based concrete incorporating single and multiple hooked-end steel fibres, J. Build. Eng. 98 (2024) 111090.

[9] C. Zhao, Z. Wang, Z. Zhu, Q. Guo, X. Wu, R. Zhao, Research on different types of fiber reinforced concrete in recent years: an overview, Constr. Build. Mater. 365 (2023) 130075.

[10] J. Esmaeili, K. Andalibi, O. Gencel, Mechanical characteristics of experimental multi-scale steel fiber reinforced polymer concrete and optimization by Taguchi methods, Constr. Build. Mater. 313 (2021) 125500.

[11] A. Plans, D. Grau, M. Soltanalipour, M. Ferrer-Ballester, F. Marimon, A. Andreu, Three-dimensional finite element modeling for bending and pull-out tests of composite slabs, Eng. Struct. 295 (2023) 116785.

[12] A. Elshinawy, M.M.Y. Elshikh, M.R. Kaloop, W.E. El-Demerdash, W.E. Elemam, An experimental investigation on mechanical characteristics of steel-fiber-reinforced volcanic concrete, Materials 6 (2025) 100308.

[13] J. Yang, B. Chen, C. Nuti, Influence of steel fiber on compressive properties of ultra-high performance fiber-reinforced concrete, Constr. Build. Mater. 302 (2021) 124104.

[14] V. Overhage, K. Heins, M. Kimm, G.-S. Ryu, Y.-J. You, H.-Y. Kim, T. Gries, Investigation of pull-out and mechanical performance of fibre reinforced concrete with recycled carbon fibres, Mater. Struct. 57 (8) (2024) 1–14.

[15] Y. Chen, Y. Jiao, H. Yang, F. Ma, J. Meng, Interfacial bond behavior of steel fibers embedded in manufactured sand-based ultra-high performance concrete, Constr. Build. Mater. 446 (2024) 138041.

[16] M. Pouraminian, A.E. Akbari Baghal, K. Andalibi, F. Khosravi, V. Arab Maleki, Enhancing the pull-out behavior of ribbed steel bars in CNT-modified UHPFRC using recycled steel fibers from waste tires: a multiscale finite element study, Sci. Rep. 14 (1) (2024) 19939.

[17] S. Guo, Y. Ding, X. Zhang, P. Xu, J. Bao, C. Zou, Tensile properties of steel fiber reinforced recycled concrete under bending and uniaxial tensile tests, J. Build. Eng. 96 (2024) 110467.

[18] Z. Que, J. Tang, H. Wei, A. Zhou, K. Wu, D. Zou, J. Yang, T. Liu, G. De Schutter, Predicting the tensile strength of ultra-high performance concrete: new insights into the synergistic effects of steel fiber geometry and distribution, Constr. Build. Mater. 444 (2024) 137822.

[19] X. Bao, Y. Li, X. Chen, H. Yang, H. Cui, Investigation on the flexural behaviour and crack propagation of hybrid steel fibre reinforced concrete with a low fibre content for tunnel structures, Constr. Build. Mater. 417 (2024) 135253.

[20] Z. Gu, J. Wang, D. Gao, J. Zhao, Effects of steel fibers on the flexural behavior of recycled concrete beam: testing and analysis, J. Build. Eng. 85 (2024) 108718.

[21] M. Li, J. Sun, L. Li, L. Meng, S. Wang, J. Wei, J. Mao, Effect of nanosilica on fiber pullout behavior and mechanical properties of strain hardening ultra-high performance concrete, Constr. Build. Mater. 367 (2023) 130255.

[22] A.A.J. Ghanim, M. Amin, A.M. Zeyad, B.A. Tayeh, I.S. Agwa, Effect of modified nano-titanium and fly ash on ultra-high-performance concrete properties, Struct. Concr. 24 (5) (2023) 6815–6832.

[23] C. Wen, P. Zhang, J. Wang, S. Hu, Influence of fibers on the mechanical properties and durability of ultra-high-performance concrete: a review, J. Build. Eng. 52 (2022) 104370.

[24] D. Ravichandran, P.R. Prem, S.K. Kaliyavaradhan, P. Ambily, Influence of fibers on fresh and hardened properties of Ultra High Performance Concrete (UHPC)—a review, J. Build. Eng. 57 (2022) 104922.

[25] D.-Y. Yoo, Y.S. Jang, B. Chun, S. Kim, Chelate effect on fiber surface morphology and its benefits on pullout and tensile behaviors of ultra-high-performance concrete, Cem. Concr. Compos. 115 (2021) 103864.

[26] J.-J. Kim, D.-Y. Yoo, N. Banthia, Benefits of curvilinear straight steel fibers on the rate-dependent pullout resistance of ultra-high-performance concrete, Cem. Concr. Compos. 118 (2021) 103965.

[27] K. Zhang, Q. Yuan, T. Huang, S. Zuo, H. Yao, Utilization of novel stranded steel fiber to enhance fiber–matrix interface of cementitious composites, Constr. Build. Mater. 369 (2023) 130525.

[28] Y. Li, F. Liu, H. Li, X. Zhang, Y. Pan, C. Liu, Pullout behavior of single arc-shaped steel fiber from brittle SIFCON matrix with various embedment lengths and inclination angles, Constr. Build. Mater. 420 (2024) 135479.

[29] Y. Li, F. Liu, Q. Li, H. Li, G. Sun, R. Liang, Effect of fiber content and end geometry on the pullout behavior of straight and arc-shaped steel fibers embedded in SIFCON, Constr. Build. Mater. 451 (2024) 138688.

[30] M. Schleiting, K. Klier, N. Wiemer, A. Wetzel, J.-C. Zarges, H.-P. Heim, B. Middendorf, Fibre pullout behaviour of fibre-reinforced UHPC with TPE-coated fibres, Constr. Build. Mater. 376 (2023) 131043.

[31] S. Ataee, M. Jalali, M.L. Nehdi, Pull-out behavior of twin-twisted steel fibers from various strength cement-based matrices, Constr. Build. Mater. 445 (2024) 137855.

[32] J.-H. Park, J.-H. Lee, E. Choi, C. Park, Effects of double-arched geometry and tensile strength on the pullout resistance of fibers, Case Stud. Constr. Mater. 19 (2023) e02316.

[33] Pourreza, T., A. Alijani, V. A. Maleki, A. Kazemi, Nonlinear vibrations of graphene nanoplates with arbitrarily orientated crack located in magnetic field using nonlocal elasticity theory. International Journal of Structural Integrity, ahead-of-print(ahead-of-print) (2025).

[34] M. Hoseinzadeh, R. Pilafkan, V.A. Maleki, Size-dependent linear and nonlinear vibration of functionally graded CNT reinforced imperfect microplates submerged in fluid medium, Ocean Eng. 268 (2023) 113257.

[35] M.H. Alizadeh, M. Ajri, V.A. Maleki, Mechanical properties prediction of ductile iron with spherical graphite using multi-scale finite element model, Phys. Scr. 98 (12) (2023) 125270.

[36] M. Rezaee, V.A. Maleki, An analytical solution for vibration analysis of carbon nanotube conveying viscose fluid embedded in visco-elastic medium, Proc. Inst. Mech. Eng., Part C J. Mech. Eng. Sci. 229 (4) (2015) 644–650.

[37] F. Akbari, M.I. Zibaii, S. Chavoshinezhad, A. Layeghi, L. Dargahi, O. Frazao, Monitoring optogenetic stimulation of light-sensitive stem cells using a twin-core fiber-based Mach-Zehnder interferometer, Opt. Fiber Technol. 88 (2024) 104024.

[38] A. Faraji, A.R. Farahani, N.B. Khoramdareh, A. Gil, S. Jafari, Z. Hekmatian, N. Shojaei, Cu-Fe nanoparticles decorated rice hull/chitosan@ FeAl2O4 to boosted peroxidase-like activity for catalytic degradation of antibiotics: kinetics and mechanistic insights, J. Environ. Chem. Eng. 11 (6) (2023) 111348.

[39] N. Rostami, A. Ghebleh, H. Noei, Z.S. Rizi, A. Moeinzadeh, A. Nikzad, M. M. Gomari, V.N. Uversky, P. Tarighi, Peptide-functionalized polymeric nanoparticles for delivery of curcumin to cancer cells, J. Drug Deliv. Sci. Technol. 102 (2024) 106337.
[40] I. Akbarzadeh, A.S. Poor, M. Khodarahmi, M. Abdihaji, A. Moammeri, S. Jafari, Z. S. Moghaddam, M. Seif, M. Moghtaderi, Z.A. Lalami, Gingerol/letrozole-loaded mesoporous silica nanoparticles for breast cancer therapy: in-silico and in-vitro studies, Microporous Mesoporous Mater. 337 (2022) 111919.
[41] N. Sharafkhani, A.Z. Kouzani, S.D. Adams, J.M. Long, J.O. Orwa, A pneumatic-based mechanism for inserting a flexible microprobe into the brain, J. Appl. Mech. 89 (3) (2022) 031010.
[42] V. Gharebagh, G. Rezazadeh, N. Sharafkhani, R. Shabani, Static and dynamic response of carbon nanotube-based nano-tweezers, Int. J. Eng. 24 (4) (2011) 377–386.
[43] M. Rezaee, N. Sharafkhani, Out-of-plane vibration of an electrostatically actuated microbeam immersed in flowing fluid, Nonlinear Dyn. 102 (1) (2020) 1–17.
[44] S. Khosravi, S. Amirsardari, M.A. Goudarzi, Dynamic Behavior of Rectangular Tanks With Limited Freeboard Under Seismic Loads: Experimental, Analytical, and Machine Learning Investigations, J. Press. Vessel Technol. 147 (2) (2025) 021901.
[45] Birtel, V. and P. Mark. Parameterised finite element modelling of RC beam shear failure. in ABAQUS users' conference. 2006.
[46] S. Bahij, S.K. Adekunle, M. Al-Osta, S. Ahmad, S.U. Al-Dulaijan, M.K. Rahman, Numerical investigation of the shear behavior of reinforced ultra-high-performance concrete beams, Struct. Concr. 19 (1) (2018) 305–317.
[47] Y.M. Abbas, Microscale cohesive-friction-based finite element model for the crack opening mechanism of hooked-end steel fiber-reinforced concrete, Materials 14 (3) (2021) 669.
[48] W.K. Liu, Y. Liu, D. Farrell, L. Zhang, X.S. Wang, Y. Fukui, N. Patankar, Y. Zhang, C. Bajaj, J. Lee, Immersed finite element method and its applications to biological systems, Comput. Methods Appl. Mech. Eng. 195 (13-16) (2006) 1722–1749.
[49] A.E.A. Baghal, A. Maleki, R.V. Sorkhabi, Finite element analysis of the adhesive behavior of shape memory alloy fiber and polymer concrete, J. Sci. Technol. Compos 7 (4) (2021) 1255–1262.
[50] P. Vahidi Pashaki, M. Pouya, V.A. Maleki, High-speed cryogenic machining of the carbon nanotube reinforced nanocomposites: finite element analysis and simulation, Proc. Inst. Mech. Eng., Part C J. Mech. Eng. Sci. 232 (11) (2018) 1927–1936.
[51] M. Ghaderi, V.A. Maleki, K. Andalibi, Retrofitting of unreinforced masonry walls under blast loading by FRP and spray on polyurea, Fen. Bilim. Derg. (CFD) 36 (4) (2015).
[52] J. Esmaeili, K. Andalibi, O. Gencel, F.K. Maleki, V.A. Maleki, Pull-out and bond-slip performance of steel fibers with various ends shapes embedded in polymer-modified concrete, Constr. Build. Mater. 271 (2021) 121531.
[53] M.P. Adams, J.H. Ideker, Influence of aggregate type on conversion and strength in calcium aluminate cement concrete, Cem. Concr. Res. 100 (2017) 284–296.
[54] R.H. Hannink, P.M. Kelly, B.C. Muddle, Transformation toughening in zirconia-containing ceramics, J. Am. Ceram. Soc. 83 (3) (2000) 461–487.
[55] L. Fei, L. Yanhuai, S. Zhongxiao, X. Kewei, Z. Zhi, C. Hong, Rietveld study on evolution of crystalline structure of ysz nanoparticles during co-precipitation synthesis, Rare Met. Mater. Eng. 44 (11) (2015) 2716–2720.
[56] M. Negahdary, A. Habibi-Tamijani, A. Asadi, S. Ayati, Synthesis of zirconia nanoparticles and their ameliorative roles as additives concrete structures, J. Chem. 2013 (1) (2013) 314862.